Generating Precise Non-Flat Grinding Wheel Surfaces via CO_2 Laser Ablation: Understanding the Relationship between Overlap Rate and Feed Rate on Composite Materials

Ke Ge Xie [a,1], Adam Rushworth [a,1,*], Hao Chen [a], Xiang Yu Zhang [b], Zhi Pei Huang [b], Yi Xiu Shen [b]

[a] *Department of Mechanical, Materials& Manufacturing Engineering, University of Nottingham Ningbo China, Ningbo 315100, China*

[b] *School of Aerospace, University of Nottingham Ningbo China, Ningbo 315100, China*

* Corresponding author. Tel.: 86 057488180000 (Ext. 8220); E-mail: Adam.Rushworth@nottingham.edu.cn

[1] These authors contributed equally to this work.

Abstract: Non-flat structures are essential features in key mechanical functional surfaces such as aero-space engine blade tenons, screw rods and machine tool guide rails etc., which usually require profile grinding as the finishing process to meet demanding working requirements. However, the precise manufacturing of profile grinding wheels remains challenging as it is hard to remove the superhard materials within the grinding wheel in a controllable way. Dressing the target wheel by laser ablation appears promising, however, the interactions between the laser energy beam and target composite materials are quite complex, especially the combined behaviours among a serial of adjacent ablation tracks are hard to understand when concerning the ever-changing Overlap Rates (ORs) and feed rates in the ablation process. In this study, the nature of the laser beam and the characteristics of the beam energy distribution are analysed. The shapes for the laser ablation under various ORs and feed rates are theoretically analysed and experimentally validated. Based on the results, empirical prediction models regarding ablation depth, width, and topography changing with ORs and feed rates are established. Finally, the possibility of manufacturing profiled grinding wheels by controlling overlap and feed rates is studied. An attempt to generate precise non-flat structures (including stepped and curved surfaces) via ablation with a CO_2 laser using the developed strategies is performed, and a smooth profile with a relative error of 2.2% is achieved without any extra focal plane change manipulations. The work provides a novel strategy for the manufacturing of complex profile grinding wheels.

Keywords: Non-Flat Grinding Wheel; CO_2 Laser Ablation; Empirical Prediction Model

1 Introduction

The need for precise manufacturing of non-flat grinding wheels has been highly emphasized due to increasingly demanding requirements in the finishing of modern, complex, functional profiled surfaces [1, 2]. This process is characterized by a need for high-precision, uniform dimensions and a large batch size. However, a number of issues closely related to the fabrication of grinding wheels with various profiles have been widely reported, e.g. difficulty of removing super hard materials [3], manufacturing precision [3, 4], and machine tool wear [5]. Therefore, exploring the proper strategies to fabricate non-flat grinding wheels in a precise, efficient manner remains an important topic to be addressed.

1.1 Applications of non-flat grinding wheels

Previously, non-flat grinding wheels have been studied for use in various scenarios (e.g. ultra-high-strength gears [6, 7], aero-space engine blade tenons [8], screw tools [9, 10], optical components [11-14], and other machine components, like dry vacuum pump rotor [15] and the groove of the ball bearing's inner ring [5]) and significant progress has been achieved.

For the manufacturing of high-performance gears, form grinding has remained one of the most important finishing methods. By changing the gear setting errors, Fang et al. [6] proposed an error compensation method to improve the form grinding accuracy for gears. Li et al. [16] proposed a function-oriented form-grinding approach to obtain excellent and stable contact performance of cylindrical gears by designing modified forms based on a predesigned controllable fourth-order Transmission Error (TE) function and error sensitivity evaluation. To optimize the gear grinding process parameters and prevent tooth surface burn, Su et al. [17] studied the temperature field of the grinding zone by using both the theoretical calculation and finite element modelling and verified the validity and feasibility of the model by metallographic analysis. By using self-developed, new micro-crystal corundum grinding wheels, Wang et al. [18] conducted experimental and theoretical analysis on the form grinding processes of 20CrMnTi steel involute gears tooth surfaces. They predicted the grinding temperature and avoided tooth burning through online detection of the tangential grinding forces. Jin et al. [19] developed a comprehensive thermal model to analyse the heat transfer mechanism in form grinding of involute gears, and Yi et al. theoretically and experimentally studied the temperature field distribution [20, 21], grinding force, heat flux, and residual stress [22] in gear form grinding. The results demonstrate that the calculated temperature distribution along the tooth profile has a rather good agreement with the measured result.

For the free form profile manufacturing, Li et al. [2] employed electroplated cubic boron nitride (CBN) profiled grinding wheels, carrying out profile grinding experiments on FGH96 turbine disk slots, high precision slot error with ±0.012 mm and low surface roughness of 0.8 μm were obtained. To enhance the wheel shape retention, suppress thermal damage, and increase the material removal rate, Zhao et al. [23] investigated the directional solidified nickel-based superalloy DZ125 with an electroplated CBN wheel. With the help of a profile-adapted needle nozzle, high shape accuracy and good surface integrity were achieved and the specific material removal rate was improved to 50 mm^3/mm, while only a slight grinding temperature variation was measured along with the profile in the grinding zone. Zhang et al. [24] investigated the wear detection of the wheel, which provides the basis for the precision NC curve point grinding strategy. Liao et al. [25] proposed a 2D wheel-profile errors model to directly compensate for 3D curved wheel errors in automatic grinding, which avoided any on-machine measurement, improved the freeform grinding accuracy and efficiency. Wang et al. [12] studied the ultra-precision grinding of the non-rotational asymmetric biconical free-form optics with a raster grinding path. By using a novel feeding compensation truing strategy, two types of grinding wheels with high profile accuracy and desired surface topography were successfully trued, a larger size monocrystalline silicon biconical free-form optics with profile accuracy 6.0 μm and nanometre surface roughness was successfully achieved. Wang et al. [13] studied the envelope grinding of micro-cylinder array lenses using a near arc-profile wheel without on-machine precision truing. Starkov et al. [26] comparatively

analysed the performance of Cubic Boron Nitride and Microcrystalline alumina tools in profile grinding of form cutter under production conditions, finding the vitrified cubic boron nitride wheel has demonstrated an essentially better performance in terms of removal rate, dressing cycles, and overall labour input. Miao et al. [8] studied the grinding force and surface quality in creep feed profile grinding of turbine blade root of nickel-based superalloy with microcrystalline alumina abrasive wheels. The results provided industry guidance to optimize the machining process for the high-valued parts with complicated profiles. Xie et al. explored the strategies to improve the accuracy of the freeform surfaces from the aspect of form-truing error compensation [27], dispersing grinding wheel profiles [28], and adjusting tool posture angle without on-machine wheel-profile truing [29]. Some researchers manage to improve the surface accuracy by path planning method, e.g., for error region grinding of aero-engine blades with the free-form surface [30] and Elastic-contact-based tool-path planning for the free-form surface in belt grinding [31].

In addition to the applications mentioned above, Bogutsky et al. [32] calculated the profile of the intermittent grinding wheel for the sharpening teeth of the broach. Chen et al. [11] studied the curvature effect on surface topography and uniform scallop height control in normal grinding of optical curved surfaces considering wheel vibration. Ichida [33] studied the performance of profile grinding of ultrafine-crystalline CBN abrasive wheels by producing V-shaped grooves on a flat surface in one pass by creep feed grinding. The study shows a 5-15% drop in grinding force and 4 times increase in grinding ratio, and high dimensional accuracy and better form retention are achieved when compared to conventional ones. Liu et al. [34] proposed a novel optimization design method for form grinding wheels for screw rotors and the effectiveness of the method is validated by the evidence that it made the screw profile significantly improved compared with the empirical method.

1.2 Grinding wheel dressing strategies

It is widely recognised that dressing strategies are the key factors that determine the surface micro/macro topography/morphology of the profile grinding wheels, which have a great influence on the machining accuracy, quality, and efficiency. Deng et al. [35] reviewed the research status and development bottleneck of various dressing methods for super abrasive grinding wheels, and point out that the efficiency and accuracy on the dressing of forming grinding wheels for complex curved parts (e.g., aerospace components, gears, and aspherical optical lenses) has been the bottleneck of wheel dressing technology.

Typically, material removal strategies are the most widespread profile dressing method that has been used, Denkena et al. [36] employed a mechanical method patterning the profile grinding wheels, and based on the which, they developed an analytical model that enables a design of patterning process of profile grinding wheels. However, in the dressing process, it shows the pattern size is significantly influenced by the patterning tool and the strategies. Therefore, some researchers explored the energy beam-based technologies, e.g., abrasive waterjet and laser. Firstly, Axinte et al. [37] reported an abrasive waterjet (AWJ) turning technology that profiling and dressing grinding wheels through the tangential movement of the jet plume, both the advantages and limitations of this technology is discussed. Deng et al. [38] carried out online efficient and precision laser profile of bronze-bonded diamond grinding wheels using a pulsed fibre laser, investigated the effects of the laser cutting depth and the track-overlap ratio of the laser cutting

on the efficiency, precision, and the quality of laser profiling. The results demonstrate that an increase in the laser cutting depth caused an increase in the material removal efficiency during the laser profiling process. The higher the laser peak power density is, the higher the surface contour precision of the grinding wheel after profiling. Notably, Guo et al. [39] employed a theoretical model guiding the laser truing process of V-shaped CBN grinding wheel and the result was experimental validated by nanosecond laser. It shows the V-shaped angle of wheel could reach 90.15° with a bottom fillet of 53 μm, while the truing time could be reduced by 72%-83% compared to mechanical method. Walter et al. [3] utilized an ultrashort pulsed laser (picosecond laser) to ablate regular micro patterns into the surface of CBN grinding tools, a high degree of control and flexibility regarding pattern geometry and the feature size is achieved, besides no significant thermal deterioration of the abrasive grits resulting from the laser process has been detected. Meanwhile, to lower the dressing cost and further improving the laser dressing efficiency, Rushworth et al. [40] tried to dress profiled grinding wheels employing a 2,000 W commercial fibre laser, and good shape accuracy was achieved despite the unwanted micro-steps.

Apart from material removal dressing strategies, some researchers investigated additive strategies, mainly (i) electroplating and (ii) brazing methods, e.g. Aurich et al. [41] applied the masking technology for the preliminary adhesion of the grains on the wheel hub so that the uniformly distributed grain pattern was achieved. Ding et al. [42] and Chen et al. [43] found the mismatch of the thermal expansion between abrasives, filler alloys, and the substrate can result in substantial residual stress, and therefore both the Cu-Sn-Ti and the Ag-Cu-Ti filler systems were separately employed to achieve a lower filler melting point. To release residual stress after brazing, Huang et al. [44] introduced the ultrasonic vibration into the diamond brazing process and successfully obtained the textured grinding wheel where not only the high bonding strength between filler alloy and diamond grits but also the high grain protrusion and therefore large chip storage were achieved. Li et al. [45] investigated induction brazing of profiled CBN wheel for grinding aerospace materials (Ti-6Al-4V). The interesting study here can be bio-inspired electroplating grinding tools generated by Yu et al. [46], where the phyllotactic pattern of the abrasives was allocated on the abrasive tool surfaces by using light-sensitive PVC together with UV exposure technology. However, these technologies are time-consuming, making them costly for general applications.

To be different, rather than working on the grinding wheels, some researchers explored the machining technique strategies on the workpiece. Zhao et al. [47] proposed a novel processing of ultrasonic vibration-assisted forming grinding gear, which provides a novel process technology for gear machining. Hsue and Chang [4] studied the synchronous hybrid micro-EDM grinding of micro-holes using helical taper tools formed by Ni-Co/diamond Co-deposition. Guo et al. investigated the water assisted pulsed laser machining with mist spray [48] and its optimisation [49] to reduce the recast layer and ensure the precision and continuity of laser machining. Tao et al. [10] studied parameter adjustment for error correction in the precise machining of screw rotor profile. Xu et al. [50] studied the fast on-machine profile characterization for grinding wheels and error compensation of wheel dressing. Although these works make up for the deficiency of the prior arts to some extent, these technologies either increased the energy cost or the additional equipment are required, which increased the whole cost of the machining.

1.3 Research gaps and aims

In conclusion, non-flat grinding wheels are important profile grinding tools for the finish machining of non-flat surfaces, such as profile grinding of gear, free-form surfaces, optical components, and other demanding surfaces, and significant progress have been achieved. However, it is widely accepted that the dressing strategies have been kept a bottleneck for the machining non-flat grinding wheels.

Thus, the aim of this paper is to generate precise non-flat profile grinding wheels via CO2 laser ablation. The ablation law regarding overlap rate and feed rate on the grinding wheel materials is investigated specifically in this study. The corresponding predictive models for the prediction of ablated topography, width, and depth are established. Based on the research results, an attempt to fabricate high-resolution non-flat surfaces by continuously controlling the overlap rate and feed rate change is demonstrated. The presented work provides a novel approach for manufacturing non-flat grinding wheels.

2 Theoretical analysis

2.1 The general ablation processes

In the ablation process, the laser beam is focused by a focus lens and the focused spot is kept still on the top surface of the resin bond diamond grinding wheel (see **Fig. 1**a). The grinding wheel can be precisely controlled by servo motors to perform rotational and transversal motions. As the focused laser beam has a high energy density, especially at the focal spot, the targeted materials will be deteriorated and removed by the intensive energy (View A in **Fig. 1**a), generating a slot related to the energy.

However, for a certainly focused laser beam, it has a focus site (see **Fig. 1**b) or focal plane (View A in **Fig. 1**a) along the laser beam propagation direction and the power density in the site is the highest. The centre laser power density decreases with the defocusing distance increase (see **Fig. 1**c) and the materials were eventually unable to be removed due to insufficient energy [51, 52]. But, the energy beam kept heating the slot boundary, allowing a Heat Affected Zone (HAZ) to form. As the bond agency is made of resin, which has a relatively lower creep deterioration temperature, HAZ also makes the ablation depth changes since the material deterioration may also occur because of the heating.

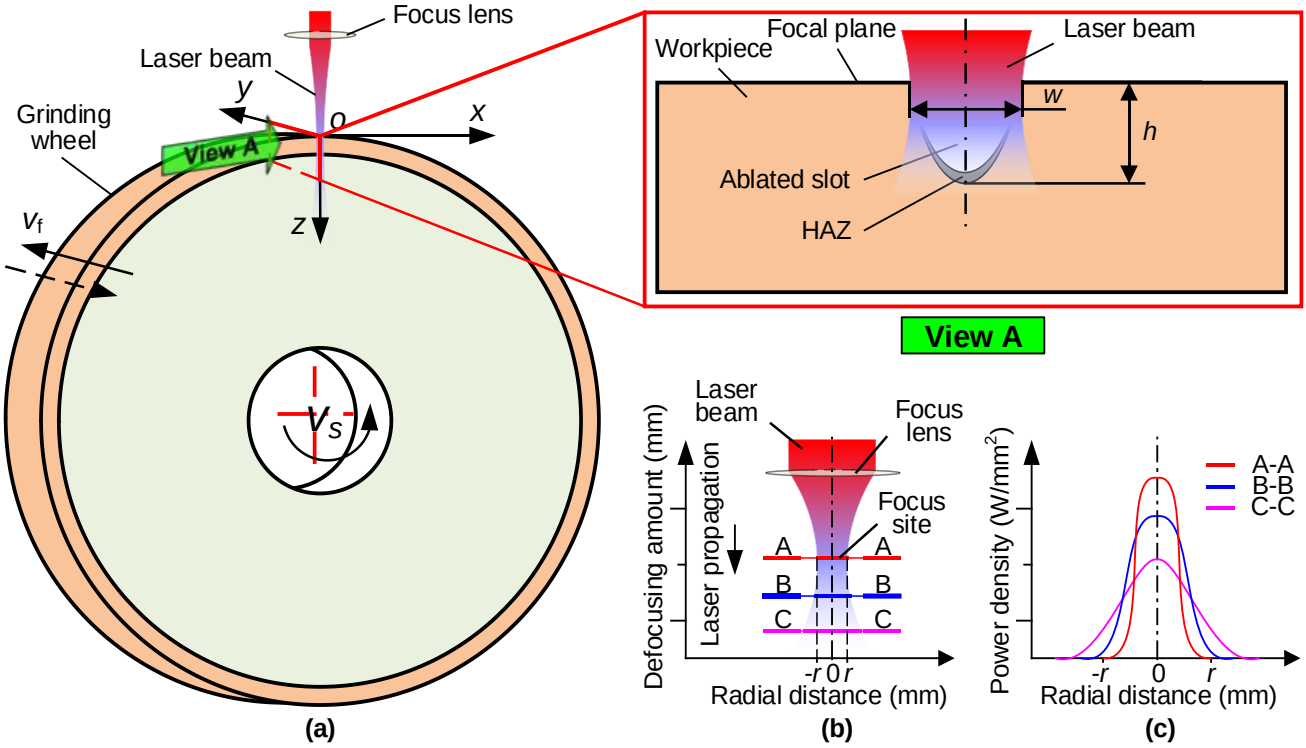

Fig. 1 Ablation process. (a) the ablation process diagram and the character of the ablated slot (View A); (b) the general shape of a focused laser beam; (c) the energy distribution at the certain cross-section along the laser propagation direction [51].

2.2 The parallel overlap ablation

Given that various energy fluences over the ablation threshold of the target material can be obtained by controlling the overlap ratio of the laser spot, various ablation behaviours could happen in the process with the overlap ratio changing [53, 54]. When no overlap (see the definition in **Fig. 2**a) in the ablation process, each laser spot is independent as little heat will be accumulated and no base shape discrepancy between the two adjacent spots (see case 1 in **Fig. 2**a). When the overlap is introduced (see case 2 in **Fig. 2**a), both the heat accumulation and base shape discrepancy start to affect the ablated topography. With the overlap ratio and ablation time increasing, the material removal behaviour tends to be more seriously affected, larger HAZ and deeper ablation depth have been found in previous studies [54, 55]. However, the ablated topographies in the stable stage are kept the same under a certain overlap ratio as the heat accumulation has a balance point, as shown in **Fig. 3**.

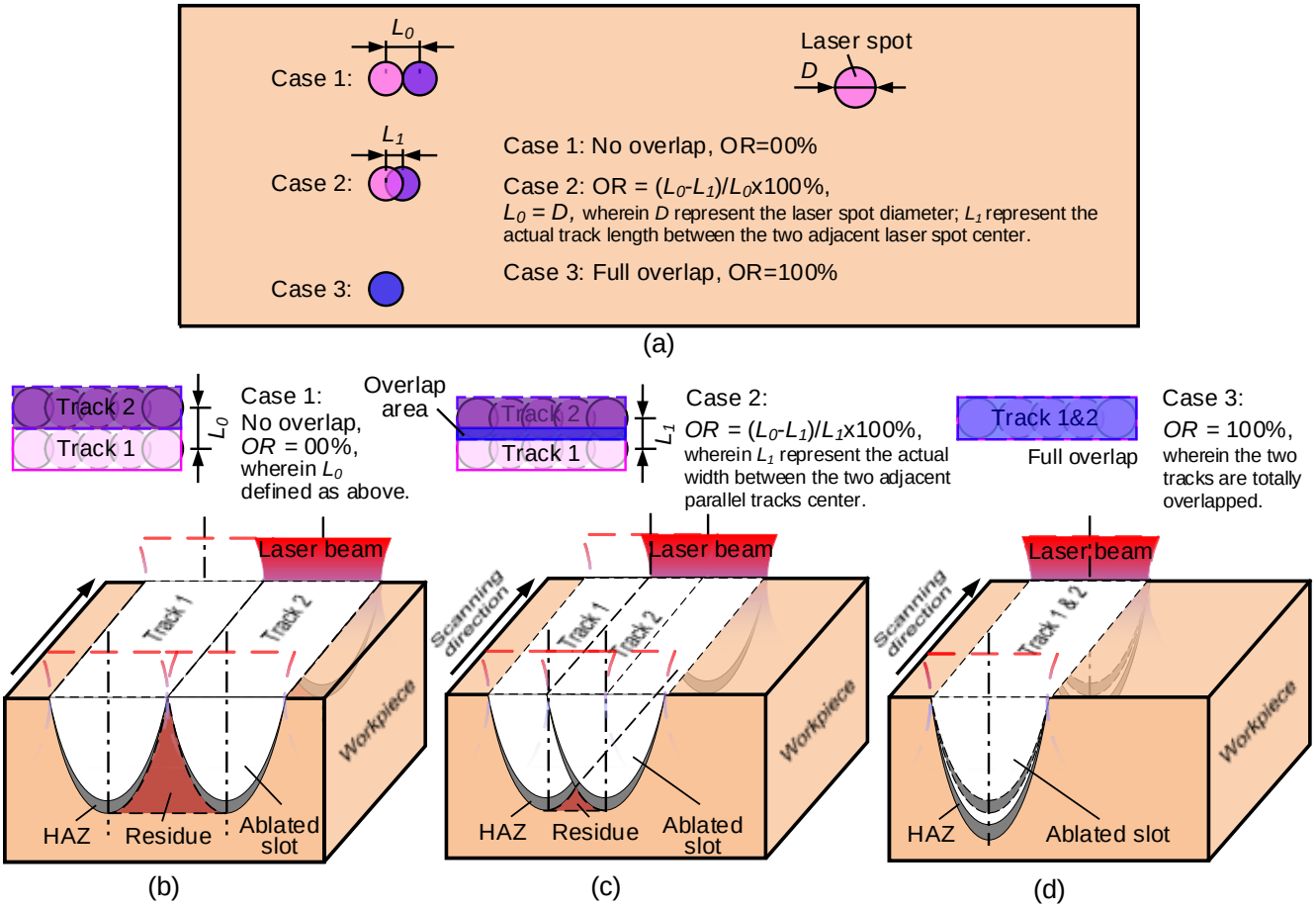

Fig. 2 Definition of overlap ablation. (a) the overlap ratio definition in single pass ablation; (b), (c) and (d) in multi-pass parallel overlap ablation.

In the parallel overlap ablation (or line overlap [56]), the laser ablation process is performed along with the previous ablated slot, the overlap ratio in different cases are defined in **Fig. 2** (b), (c) and (d). As no parallel overlap happen when the distance between the adjacent tracks is over the spot diameter, the ablation track intervals between the two slots are normally equal to or smaller than the diameter of the spot. By the methodology of analogy, it can be found that the parallel overlap ablation is an extension for single-pass overlap ablation from an array to a matrix. Differently, as heat generated in track 1 usually has little effect on track 2, most of the heat-related issues (including the incubation effect [57]) rarely happen in parallel overlap ablation. Therefore, the topography in parallel overlap ablation is little affected by the heat accumulation but is close affected by the base shape and overlap ratio of two laser tracks.

Based on the theoretical analysis above, here further predicted the topographies of five parallel overlap passes (the ablated slots do not change much after 5 passes, see **Fig. 3**) under various cases from OR 00% to OR 100% with an interval of 20%, as showing below:

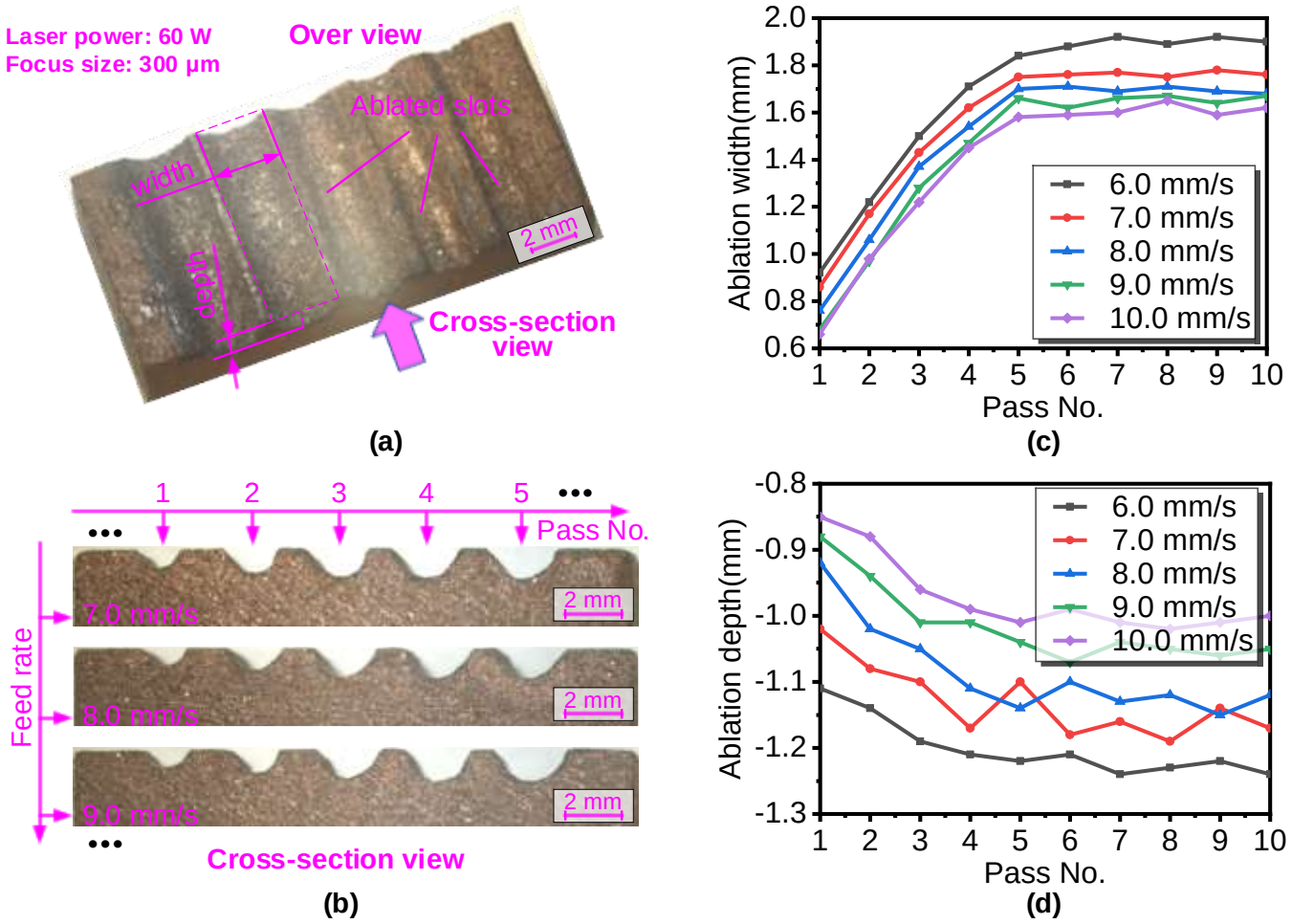

Fig. 3 Ablation results after multiple passes. (a) and (b) the physical model of the ablated samples; (c) and (d) The ablation width and depth changes with feed rate and pass number under laser power 60 W.

(1) When the OR is lower or equal to 50%, like the case OR 00% (see **Fig. 4**a), as no overlap happened between the two adjacent tracks, the two tracks have little effect on each other. Hence, the superposition of the two tracks will not cause ablation depth changes. For the case OR 20% (see **Fig. 4**b) and the case OR 40% (see **Fig. 4**c), although a certain amount of overlap has occurred, the power density in the bottom of the slot is low due to defocusing effect (especially off the centre of the laser beam), which indicates the ablation depth of the superposed two tracks will not be dramatically changed. Thus, the ablation depth is not likely to change significantly when the OR is less than 50%.

(2) When the OR exceed 50%, the ablation process starts to slightly increase the ablation depth (see **Fig. 4**d to **Fig. 4**f) due to (i) the relative higher power density in the current beam centre being close to the previous ablated slot bottom, (ii) the previous ablated slot enables the current laser beam directly reach to the bottom of the slot. Finally, when the OR increases to 100% (two tracks are fully overlapped), the residues between the two tracks disappeared (see **Fig. 4**f). Meanwhile, the final ablated depth of the fully overlapped ablation will not be equal to the sum of the independent ablation depths since the power density in the section changes along the laser beam propagation direction.

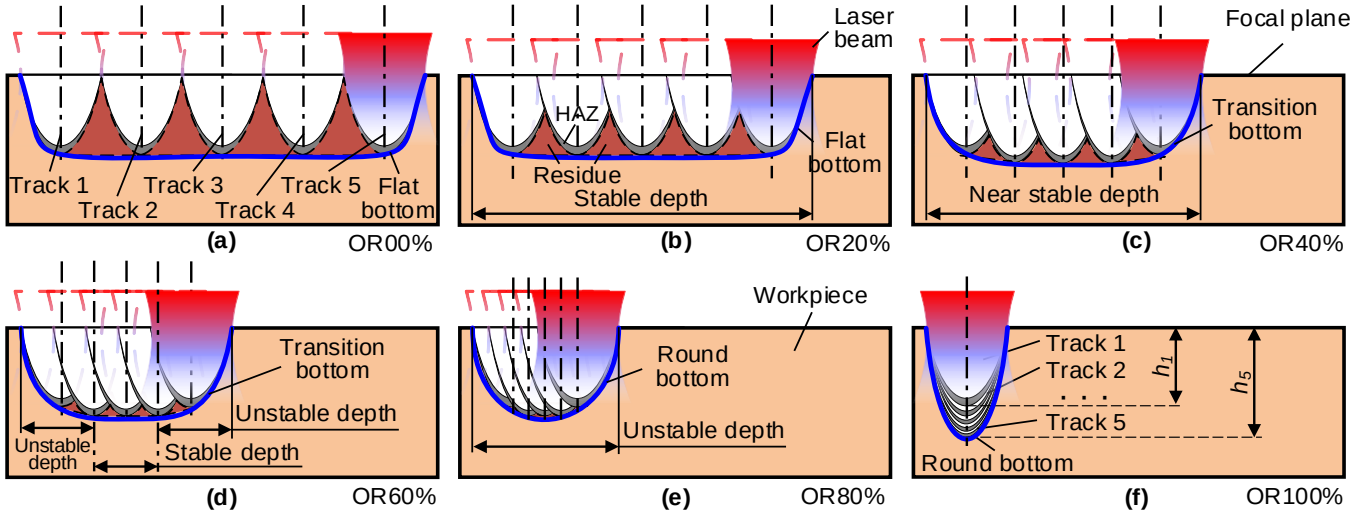

Fig. 4 Diagram of parallel overlap ablation. (a) no overlap (OR 00%); (b) less than half overlap (OR 20%); (c) less than half overlap (40%); (d) over than half overlap (60%); (e) over than half overlap (80%); total overlap (100%).

Theoretically, with the overlap rate (OR) increase (track intervals decrease), the ablation residue is reduced from the highest level at OR 00% to the lowest at OR 100%. Actually, when taking into consideration the size effect, heat accumulation, and heat impact, the ablation residues between the tracks are hard to be detected. Three major reasons may account for the issue, (i) the residual between the two tracks usually has a small volume and a big heat convection surface area, the size effect makes these small structures easily to be heated, (ii) the heat accumulation process is easier to happen in the bottom of the ablation, which furthermore heated these small structures, and (iii) these small structures are also can damaged by the intensively transient heat impact. The disappearing of the ablation residues would likely interest the ablation results that a flat, transition and round bottom can be obtained by employing the ORs that are much smaller than 50% (see **Fig. 4**a & b), near around 50% (see **Fig. 4**c & d), and much bigger than 50% (see **Fig. 4**e & f), respectively.

In conclusion, due to the nature of laser beam energy distribution, the ablated topography types are very limited for a single track, especially the bottom shapes. However, as both the nature of the laser beam energy distribution and the laser parallel overlap rate would have a crucial effect on the ablated profile (the dominant effect of overlap ablation can be changed by controlling the ORs), the ablated topography (including the width, depth, and shape) can be largely extended by overlap ablation. With this, it is clear that some general applications regarding non-flat grinding wheels (e.g., the stepped/free-form surface) can be obtained by selecting the appropriate ORs.

3 Experimental investigation

3.1 Experimental methodology

The layout of the experimental system is shown in **Fig. 5** (a), which involves a laser machine (including laser control PC and laser machine body), a positioning system (including motion body and motion controller), and a laser distance sensor (including laser distance sensor and PC). The linear and circular motions and positions for the ablation process were accurately controlled by the specially-made positioning system (see **View A** in **Fig. 5**a), which has the translational and

the rotational motion accuracies of 1 μm and 0.009 deg based on the G-code-based NC system. The translational and rotational motion speeds were separately within the ranges of 0~1,500 mm/s and 0~1,800 deg/s. The radial runout error of the grinding wheel is precisely detected by the laser distance sensor, and manually-adjusted till the runout error is within 0.01 mm.

The continuous-wave carbon dioxide laser generator (LE900, Hongfan Tech. Company) is employed (The specific of the generator is shown in **Tab. 1**).

Tab. 1 Details of the carbon dioxide laser generator.

Maximum power (W)	Wavelength (μm)	Repeat frequency (Hz)	Focal spot (mm)	Focal length (mm)
60	10.6	5000	0.3	12.5

A commercial red semiconductor laser distance sensor (MSE-TS803-60/10, Moduloc System Engineering Ltd.) is used in this study (see more details in **Tab. 2**).

Tab. 2 Details of the laser distance sensor.

Range (mm)	Linearity (F.S)	Resolution (F.S)	Temperature drift (F.S /°C)	Frequency (Hz)
10	±0.05%	0.01%	0.02%	Max.9400

The standard commercial resin bond diamond grinding wheels (D125N75B771/8, 3M Company) is used in all the trials in this study (see more details in **Tab. 3**).

Tab. 3 Details of the used diamond abrasive grinding wheels in the trial.

Shape	Size (mm)	Abrasive type	Mesh No. (#)	Hardness	Abrasive density (vol.%)	Bond
plate	Φ125×Φ32×20	Diamond	120	N	75%	phenolic resin

As this paper aims to study the effects of ORs on the ablated depth under various feed rates, wide ranges of both the OR and feed rate were employed. To make the results comparable, all the trials using six different levels of ORs and six levels of laser feed rates were performed on one diamond wheel surface in the air atmosphere. As shown in **Fig. 5** (b), the whole wheel was equally divided into six segments (see samples A to F) along with the wheel circumferential direction and in each sample, there were six ablated tracks along the wheel axis direction (OR00%-OR100% with an interval of 20%). The laser feed rate was incrementally increased from segment A (5.0 mm/s) to F (10.0 mm/s) based on our previously study [58]. The tracks OR was incrementally increased from the OR 00% to OR 100% and there are 5 parallel passes for each OR (see **View B** and **View C** in **Fig. 5**b). The used parameters were given in **Tab. 4.**

Tab. 4 Employed laser parameters in the trials.

Trial No.	ORs(%)	Feed rate (mm/s)	Segment No.	Trial No.	ORs(%)	Feed rate (mm/s)	Segment No.
1-6	100,80,	5.0	A	19-24	100,80,	8.0	D
7-12	60,40,	6.0	B	25-30	60,40,	9.0	E
13-18	20,00	7.0	C	31-36	20,00	10.0	F

After the laser ablation process, the diamond grinding wheel was firstly cut into 6 samples (A-F) by the wire-EDM machine (MV2400S, Mitsubishi Electric Company), and the two cross-sections of each sample were carefully polished by the polisher (Yuzhou Company) with alumina sizes of #320 (1 hour), #600 (1 hour) and #1,200 (3 hours). After that, each sample was cleaned by a hairbrush and ultrasonic distilled water bath for 1 hour and then air-dried at room temperature. Then the optical microscopy (NSZ-810, NOVEL OPTICS) was performed to observe and measure the ablated slots (see **Fig. 5**c), where the ablated top width (*W*), the bottom depth (*H*), and the

topography are recorded. Then the second-order regression prediction model is established based on the ablated top width and bottom depth. Besides, the topography was fitted by the nine key points on the observed cross-section profiles based on super-Gaussian and polynomial functions. The nine key points including one deepest valley point (where the depth was *h*, see the Point P5), two endpoints (see the Point P1 and P9), and six intersecting points between the cross-section profile and the horizontal lines having the depth of 20%, 60% and 90% of *h* (see the Point P2- P4 and P6- P8). The top width and bottom depth are separately defined as the distance of the two endpoints (P1 and P9) and the vertical distance of the endpoint (P1 or P9) to the deepest valley point (P5), see **View D** in **Fig. 5** (c).

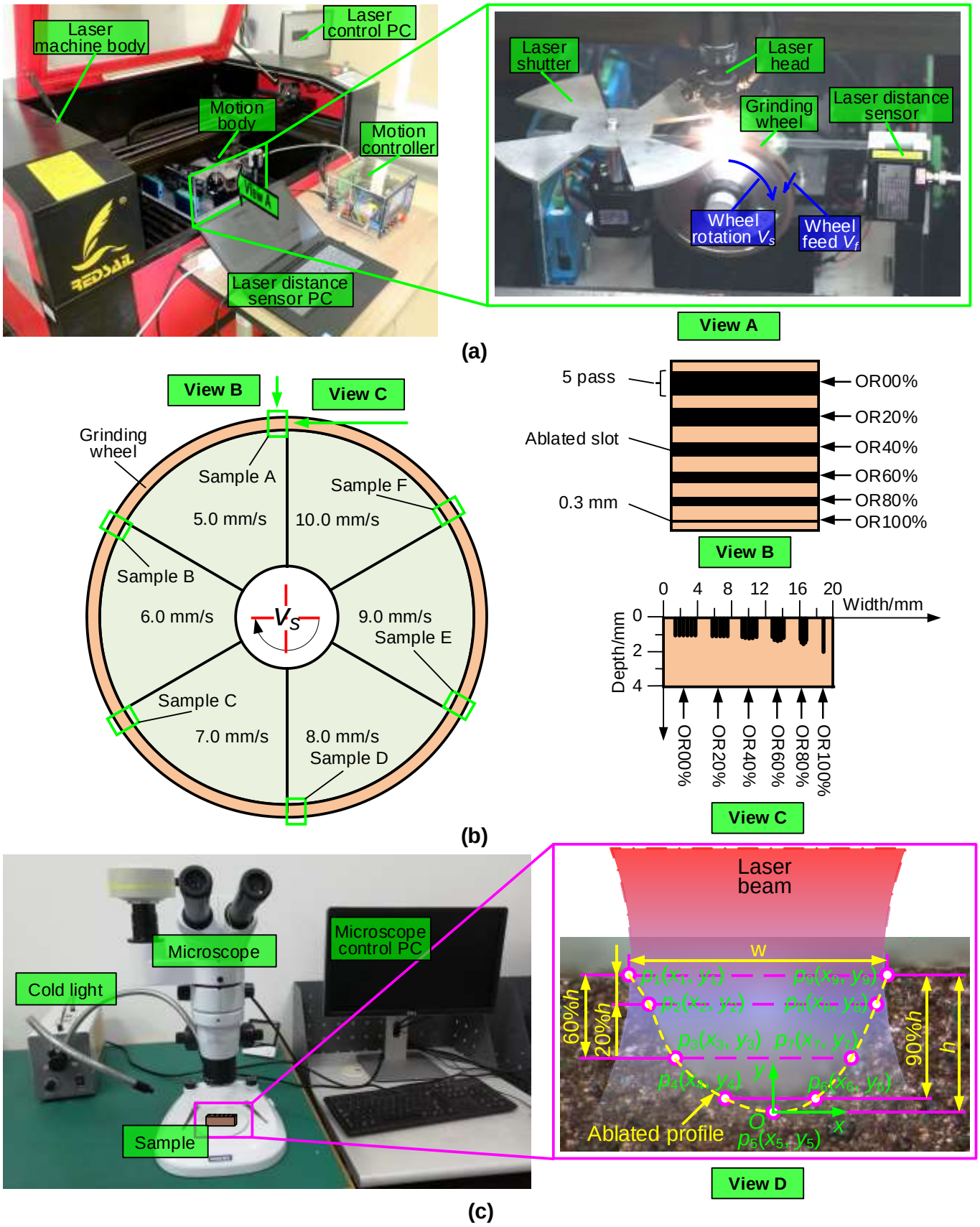

Fig. 5 Experiment methodology. (a) experimental setup including the laser machine (left) and the specially-designed positioning system (right); (b) the ablation strategy where the wheel was equally divided into six segments (A-F) and in each segment there were six ablated tracks along the wheel axis direction (OR 00 % - OR 100% with an interval of 20%, where OR refers to Overlap Rate). The laser feed rate was incrementally increased from segment A (5.0 mm/s) to F (10.0 mm/s), while the tracks OR was incrementally increased from the OR 00% to OR 100% and there are 5 parallel passes for each OR; (c)

the measurement system for the ablated slots, and the nine key points that the ablated width (*W*), depth (*H*) and topography are based to be recorded.

3.2 Experimental results and analysis

The detailed ablation results (for 60 W laser power) with duty cycle and feed rate change are recorded and analysed, where the Overlap Rate (OR) changes from 00% to 100% with an interval of 20% and Feed Rate changes from 5.0 mm/s to 10.0 mm/s with an interval of 1.0 mm/s. Both the data for ablated top width (TW) and bottom depth (BD) have been collected, and the ablated topography is analysed as well. Based on the data, the ablation law regarding TW and BD change with overlap rate and feed rate are achieved, and then the corresponding empirical prediction model has been established.

3.2.1 The influence on the ablated topography under varying feed rates and overlap rates

As expected, nearly no residuals can be found in the whole cases of the experimental process thanks to the strong laser heat that destroyed the micro-structures between the two passes. Besides, the feed rates seem to change little of the ablated bottom shape, they only narrow the ablation width and shallow the ablation depth with the feed rates increase under certain OR (see feed rate 5.0 mm/s in **Fig. 6**a to feed rate 10.0 mm/s in **Fig. 6**f). This phenomenon may account for that the feed rate changes the energy intensity on the whole, but the energy distribution state in the laser beam cross-section is kept unchanged, which is determined by the nature of the laser beam. As the laser energy distribution in a certain laser beam cross-section does not change, the ablated profile will not change as well. However, due to the whole energy intensity becoming weaker, both the ablation width and depth were reduced.

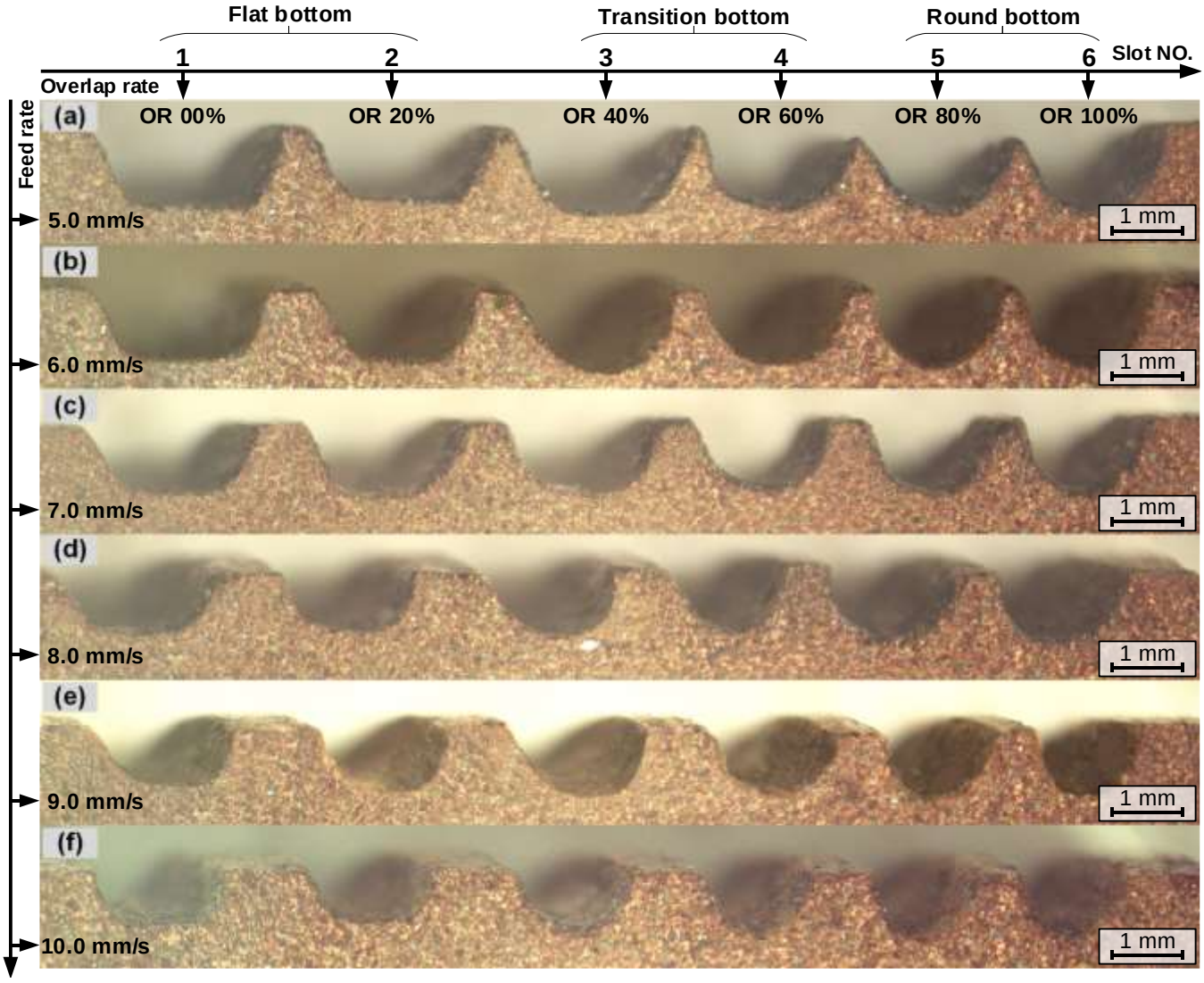

Fig. 6 The influence on the ablated topography under varying feed rates and overlap rates. (a)-(f) refer to feed rate of 5.0 mm/s, 6.0 mm/s, 7.0 mm/s, 8.0 mm/s, 9.0 mm/s, 10.0 mm/s, respectively. Slot No. 1-No. 6 refer to the overlap rate from 00% to 100% with an interval of 20%, where OR 00% and OR 20% showed a flat bottom, OR 40% and OR 60% showed a transition bottom, and OR 80% and OR 100% showed a round bottom.

Interestingly, the topography of the ablated slot bottom changes with the OR under the whole used feed rates, from flat bottom, via transition bottom, to round bottom (see slot 1 to slot 6 in **Fig. 6**). To be specific, when the OR is far less than 50% the bottom of the slots tend to be flat, while they tend to be round when the OR is far over 50%, and they tend to be transition bottom when the OR is near 50%. This is likely due to the dominating effect of overlap that when the neighbouring two laser passes are far (say far less than 50%), the current laser pass has little effect on the previous one. As a result, each pass's ablation process is relatively independent and the removal depth is the same. With the OR becoming larger, the neighbouring two passes become close, especially the intensive energy distributed in the laser beam centre overlapped, the ablation depth will change dramatically as the laser beam in the current pass will reach the bottom directly since the previous pass has removed part of the materials.

3.2.2 The influence of overlap rate changes on the ablation law under different feed rates

Fig. 7 (a) shows the ablation width decreases with the ORs increase under all the feed rates. However, the overlap rate effect ablation width in a different way under various feed rates that the ablation width has a wide variation range under lower feed rate. The ablation width decreased 1.06 mm (from 2.86 mm to 1.80 mm) for 5.0 mm/s when the OR changes from 00% to 100%, while the data for 10.0 mm/s only decreased 0.35 mm (from 2.00 mm to 1.65 mm). There is no doubt that the ablation width decreased with the ORs increase as the reduced parallel track intervals make the effective sum width of the tricks narrow. Due to more heat would be accumulated in low feed rate that enlarges the heat affect zone, which would further extend the ablation width. Thus, it makes the variation range larger in the low feed rate than that in the high.

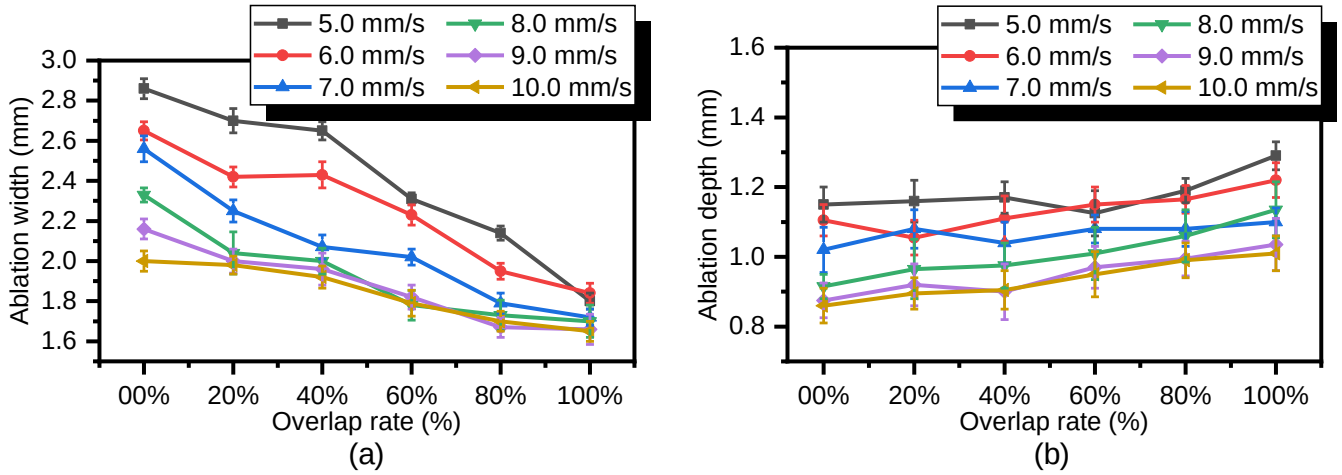

Fig. 7 The influence of overlap rate changes on the ablation law under different feed rates. (a) the effect of overlap rate on ablation width;(b) the effect of overlap rate on ablation depth.

As the figure for ablation depth, Fig. 7 (b) shows it overall has a climbing tendency with the overlap rate increased at any feed rates, and deeper ablation depth can be achieved under a lower feed rate, as expected. Surprisingly, the overlap rate seems to affect equally the ablation depth (a 0.15 mm average fluctuation is found for each feed rate). Interestingly, the ablation depth is kept almost unchanged (average increased by 3.13%) when the overlap rate is lower than 50%, but the ablation depth shows a fast growth (average increased by 7.79%) when the overlap rate is over 50%, doubled the grows rates in lower overlap rate. It's not hard to understand the phenomenon, as the two adjacent tracks have little effect on each other when the overlap rate is low. With the overlap rate increase, the mutual effect between the two adjacent tracks becomes intensive, which causes the ablation depth to begin to change dramatically. However, for the limited ablation depth change, it is likely due to the dual role of the defocusing effect of the laser beam that is determined by its nature and the narrowed ablation slot caused by the increased overlap rate.

3.2.3 The influence of feed rate changes on the ablation law under different overlap rates

Fig. 8 (a) shows the ablation width decreases with the feed rates increase under all the ORs. To be different, the feed rate effect ablation width more violently under a lower overlap rate that a maximum fluctuation of 0.86 mm is found for OR 00% when the feed rate changes from 5.0 mm/s

to 10.0 mm/s, while the figure for OR 100% only decreased 0.15 mm from 1.80 mm to 1.65 mm, which almost keep unchanged. Undoubtedly, as the heat affect zone will be decreased with the feed rate increase due to less heat will be accumulated in the ablated area. Meanwhile, with the overlap rate increase, the effect scope is getting narrow, hence the feed rate shows a negative correlation to the ablation width, and a moderate fluctuation range appears in a higher overlap rate.

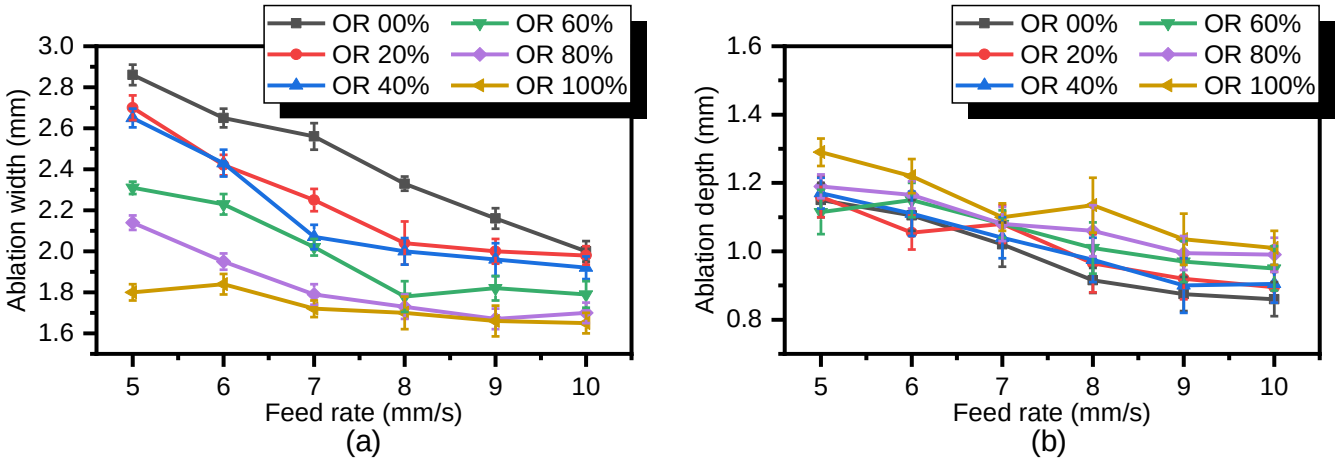

Fig. 8 The influence of feed rate changes on the ablation law under different overlap rates. (a) the effect of feed rate on ablation width; (b) the effect of feed rate on ablation depth.

Fig. 8 (b) shows the whole trend of ablation depth reduced slightly with the feed rate growing under the trialled ORs, and higher ablation depth appears in low feed rate with high OR (a maximum drop of 0.30 mm is found in feed rate 5.0 mm/s with OR 100%). Interestingly, the feed rate seems to affect almost equally the ablation depth under the trailed ORs, to be specific, the average drop for all trails is 0.24 mm with a maximum variation of 0.06 mm. It is easy to be understood that the ablation depth is reduced with the feed rate increase, as the increased feed rate reduced the laser energy fluence, which is crucial to the ablation process. As for the effect of feed rate work on the ablation depth, it is likely due to the feed rate changed laser energy fluence, which puts a similar effect on the ablation cases with various ORs. Meanwhile, the defocusing effect of the laser beam that determined by its nature and the narrowed ablation slot caused by the increased overlap rate. As a result, the ablation depth drops at a similar trend with the feed rate increases under the trailed ORs, and the ablation depth appears deeper in low feed rate with high OR.

In short, the experimental results are consistent with the theoretical analysis. The profiles of the ablated topography are close related to the OR, by controlling the OR changes from 00% to 100%, the bottom shape of the slots can be changed from flat to round. Meanwhile, the feed rate changes little of the profile, but with the feed rate increase, both the ablation width and depth are reduced. With the law, the possibility to generate desired stepped surfaces and curved surfaces by selecting the proper processing parameters can be validated.

3.3 Empirical prediction model

As the ablated results are determined by the overlap rate and feed rate in this study, a second-order regression equation is employed to establish the prediction model. The effectiveness of this model in solving practical problems has been proved in the previous study, which has shown a

pleasant result [59]. The standard form of second-order regression prediction model of two interaction factors is given by Eq. (1):

$$f(x_1, x_2) = \varepsilon + \beta_1 x_1 + \beta_2 x_2 + \beta_{12} x_1 x_2 + \beta_{11} x_1^2 + \beta_{22} x_2^2 \quad (1)$$

Where: x_1 is the overlap rate (%), and x_2 is the feed rate (mm/s).

3.3.1 Prediction model for ablated width and depth

By fitting the data with the second-order regression prediction model, the ablation width changes with overlap rate and feed rate are expressed as Eq. (2):

$$f_1(x_1, x_2) = 4.739 - 1.666e^{-2}x_1 - 4.578e^{-1}x_2 + 5.357e^{-6}x_1^2 + 1.223e^{-3}x_1 x_2 + 1.875e^{-2}x_2^2 \quad (2)$$

where: x_1 represents the overlap rate (%), x_2 represents the feed rate (mm/s), and $f_1(x_1, x_2)$ represents the ablation width (mm).

Fig. 9 (a) shows the overview prediction result of ablation width changes with overlap rate and feed rate, which indicate the ablation width decreases with both the increase of overlap rate and feed rate. **Fig. 9** (b) and (c) show the side view of overlap rate and feed rate influence on the ablation width, respectively. They shown the overlap rate linearly affect the ablation width while the feed rate non-linearly affects the ablation width.

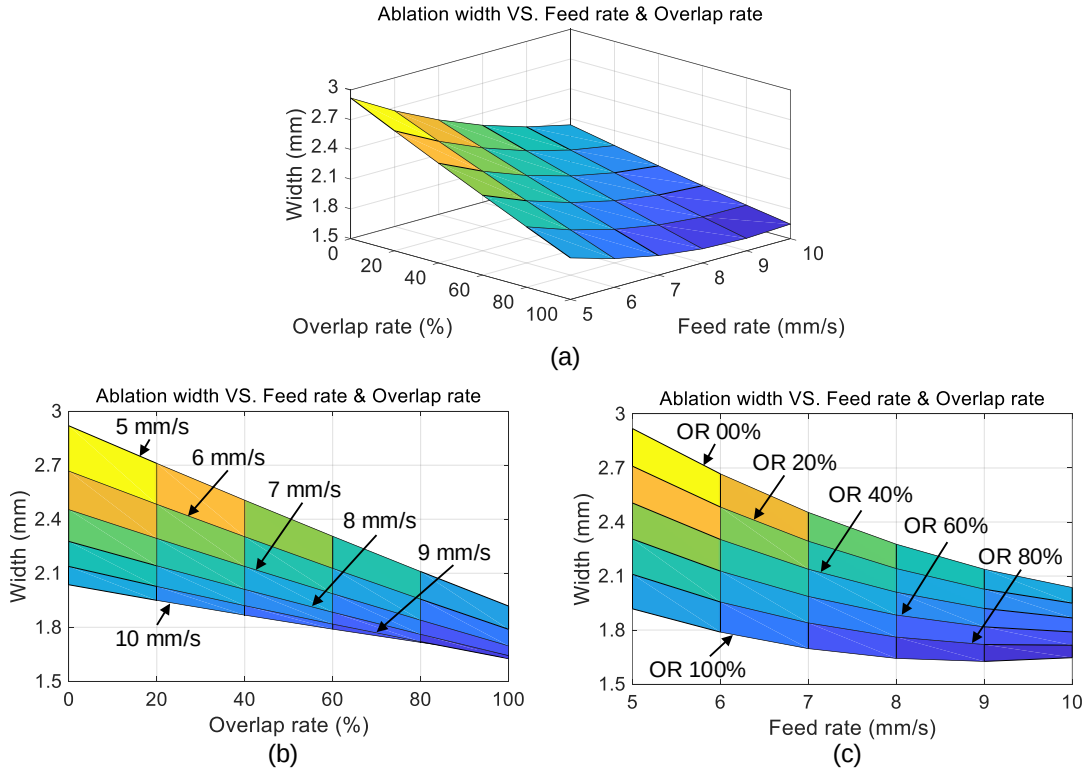

Fig. 9 Ablation width changes with overlap rate and feed rate. (a) The overview of the prediction result; (b) The influence of overlap rate on ablation width; (c) The influence of feed rate on ablation width.

By using the same fitting method, the second-order regression prediction model regarding the ablation depth changes with overlap rate and feed rate is expressed as Eq. (3):

$$f_2(x_1, x_2) = 1.605 - 8.652e^{-4}x_1 - 1.055e^{-1}x_2 + 1.213e^{-5}x_1^2 + 1.343e^{-4}x_1 x_2 + 3.065e^{-3}x_2^2 \quad (3)$$

where: x_1 represents the overlap rate (%), x_2 represents the feed rate (mm/s), and $f_2(x_1, x_2)$ represents the ablation depth (mm).

Fig. 10 (a) shows the overview prediction result of ablation depth changes with overlap rate and feed rate, which indicate the ablation depth reduces with the feed rate increase and the decreases

of overlap rate. **Fig. 10** (b) and (c) show the side view of overlap rate and feed rate influence on the ablation depth, respectively. They indicate that both the overlap rate and feed rate non-linearly affect the ablation depth, and the ablation depth has a larger fluctuation range under a given overlap rate than that under a given feed rate.

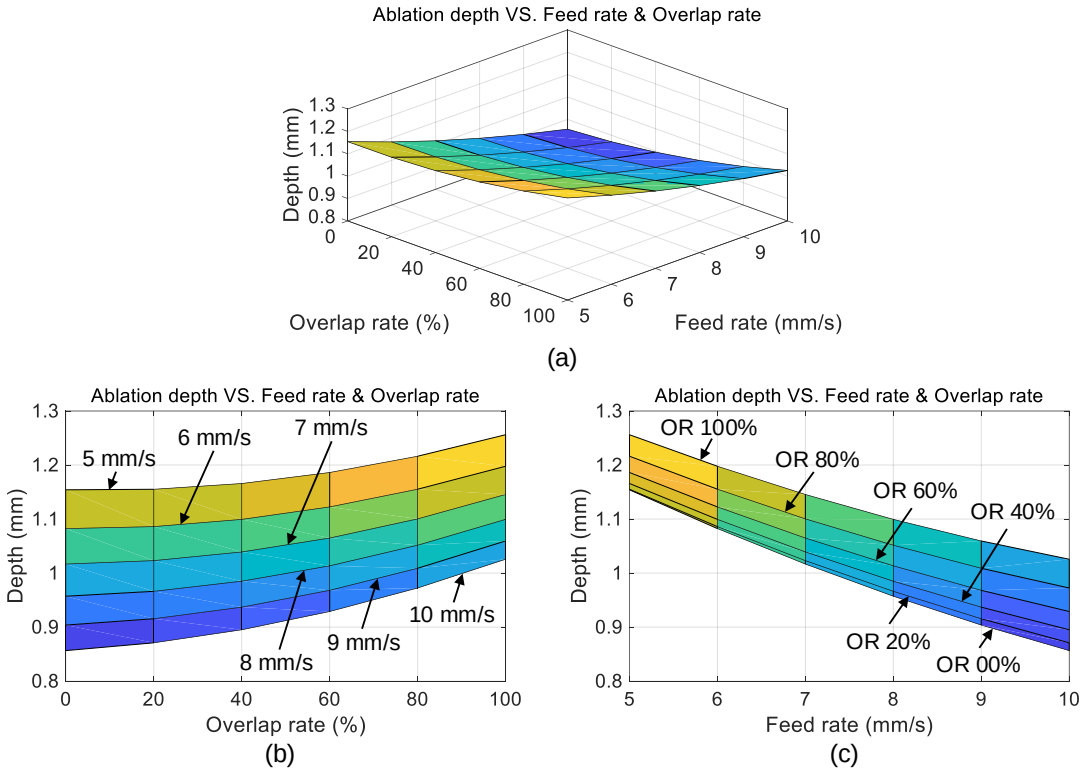

Fig. 10 Ablation depth changes with overlap rate and feed rate. (a) The overview of the prediction result; (b) The influence of overlap rate on ablation depth; (c) The influence of feed rate on ablation depth.

The goodness of fit of the two empirical prediction models is evaluated as shown in **Tab. 5**. It shows the Sum of Squares due to Error (SSE) and the Root Mean Squared Error (RMSE) tend to be zero. Both the two prediction models' confidence level is over 95%, and the Coefficient of determination (R-square) for the two models is 0.9693 and 0.9411, respectively. These signs indicate the predicted results are credible and desirable.

Tab. 5 Goodness of fit.

No.	Prediction Models	SSE	RMSE	R-square	Confidence level
1	$f_1(x_1, x_2)$	0.1168	0.0624	0.9693	> 95%
2	$f_2(x_1, x_2)$	0.02373	0.02812	0.9411	> 95%

3.3.2 Prediction model for ablated topography

Fig. 11 shows the fitted profile of each ablated topography with 95% confidence bounds, where the **Fig. 11** (a) - (d) are fitted by the Super Gauss formula as their bottom tend to be flat, **Fig. 11** (e) is fitted by unary quartic polynomial due to the round bottom and the slight asymmetry profile, and **Fig. 11** (f) is fitted with quadratic polynomial for its round bottom and symmetry profile.

With the overlap increases, it shows the whole ablation widths become narrow and the ablation depths become deep. Meanwhile, the bottom shapes gradually change from flat to round. As expected, these basic characteristics trends are consistent with the experimental results.

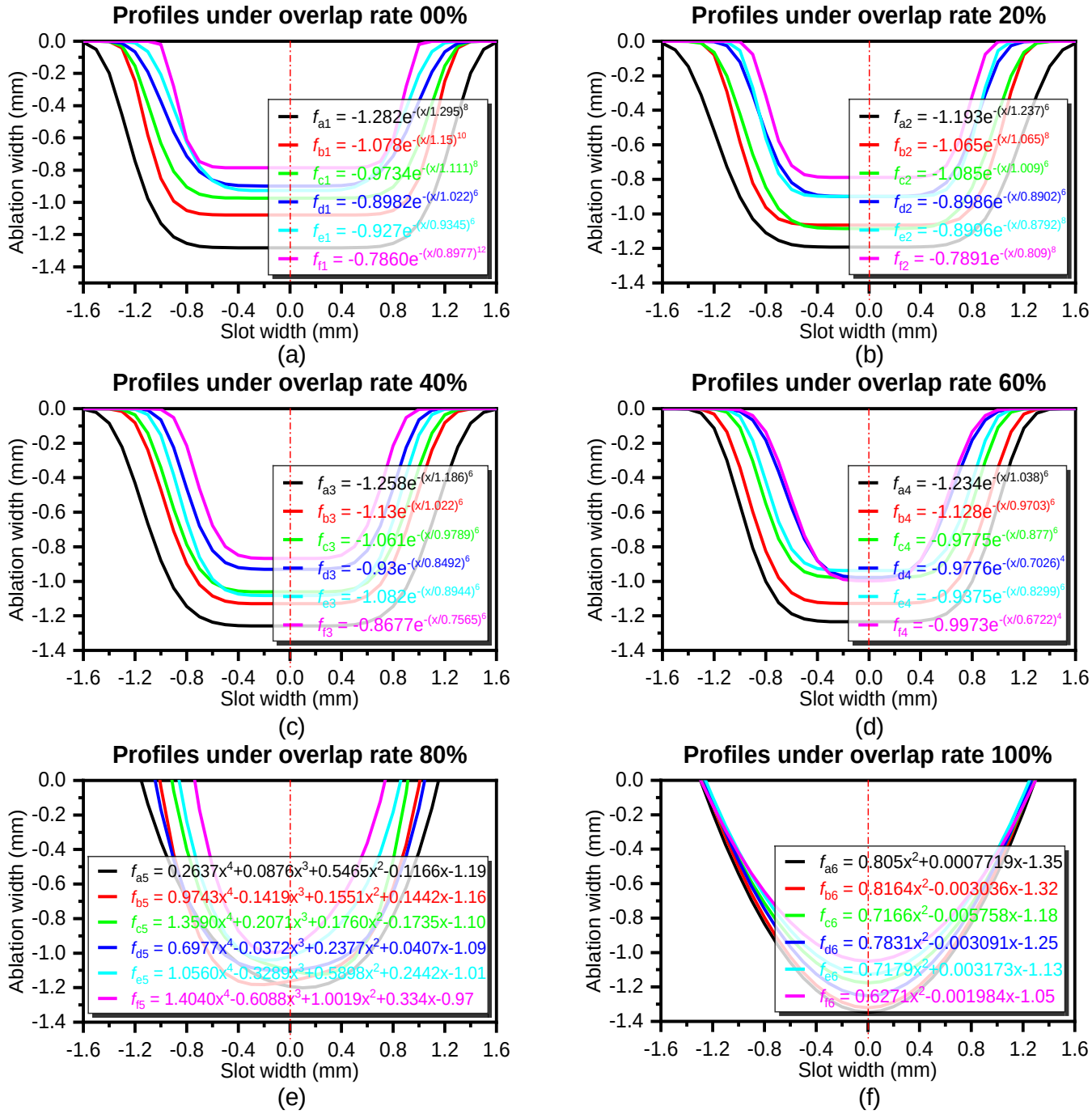

Fig. 11 The fitted profile of the ablated topography with 95% confidence bounds. (a), (b) flat bottoms generated by overlap rates 00% and 20% (fitted by Super Gauss Formula); (c), (d) transition bottoms generated by overlap rates 40% and 60% (fitted by Super Gauss formula); (e), (f) round bottoms generated by overlap rates 80% and 100% (fitted by Polynomial). Wherein, the alphabetic subscript (a-f) and numeric subscript (1-6) in the fitting functions (f_{xx}) represent feed rates (5.0 mm/s - 10.0 mm/s, increased by 1 mm/s) and ORs (00% - 100%, increased by 20%), respectively.

To further understand the correctness of the prediction model, the goodness of fit for each profile is also analyzed, as shown in **Fig. 12.** Despite there being also some worst situations that the R-square results are lower than 90%, these figures all show the acceptance of the prediction model. To be specific, the maximum SSE and RMSE are 0.142 (see **Fig. 12**a) and 0.154 (see **Fig. 12**b), respectively. Meanwhile, the R-square in most of the cases are over 96% (see **Fig. 12**c), even in the worst situation, the lowest R-square result is 89% (located in OR 40% in **Fig. 12**c). Actually, the worst predictions are all distributed in the process situation OR 40% and OR 60%, e.g. 89%,

91% shown in process situation OR 40%, and 94%, 95% shown in process situation OR 60%, this is likely due to the sake of irregular transition bottom shape cased the poor fit of the prediction results.

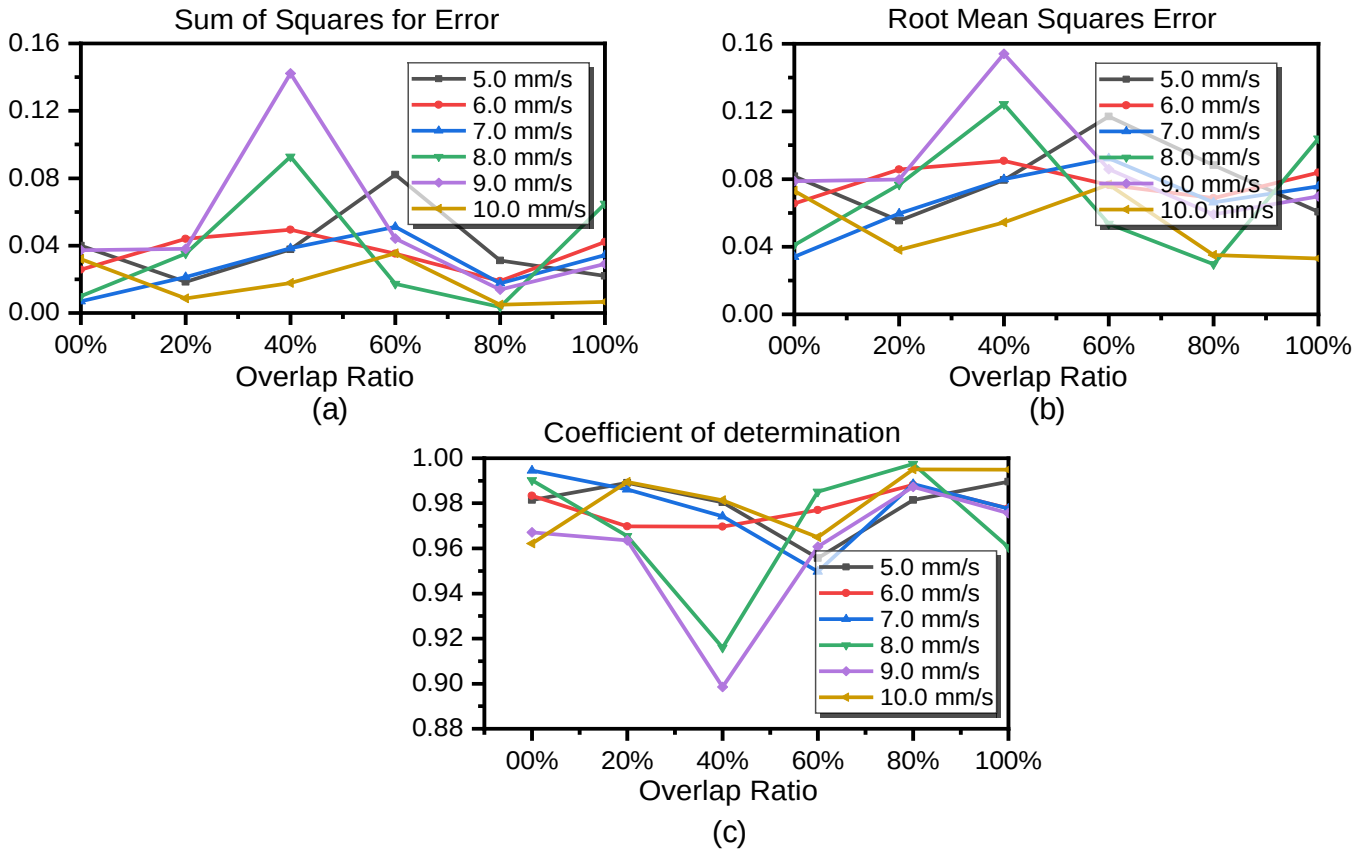

Fig. 12 Goodness of the fitted profiles. (a)-(c) the Sum of Squares for Error (SSE), Root Mean Square Error (RMSE), Coefficient of Determination (R-square) changes for each feed rate under various overlap rates, respectively.

4 Applications

Based on the research results, an attempt to manufacture two kinds of high-resolution non-flat surfaces (multi-steps and free forms) by controlling the focal plane, the overlap rate and feed rate are demonstrated, which is the usage of the knowledge above to select the proper ablation parameters for the generation of the desired profile.

The ablation strategies can be explained by **Fig. 13**, where the laser power of 60 W is employed throughout the experiments, the Focal plane (FP), overlap rate and feed rate are taken as the variables to achieve a wide range of ablation topography. Wherein, the overlap rate and feed rate are respectively controlled by axial moving speed and rotational speed of the grinding wheel manipulated by a precision positioning system, while other ablation parameters are kept unchanged. According to the designed profile, a serial of processing parameters are carefully selected for each feature based on the predictive models.

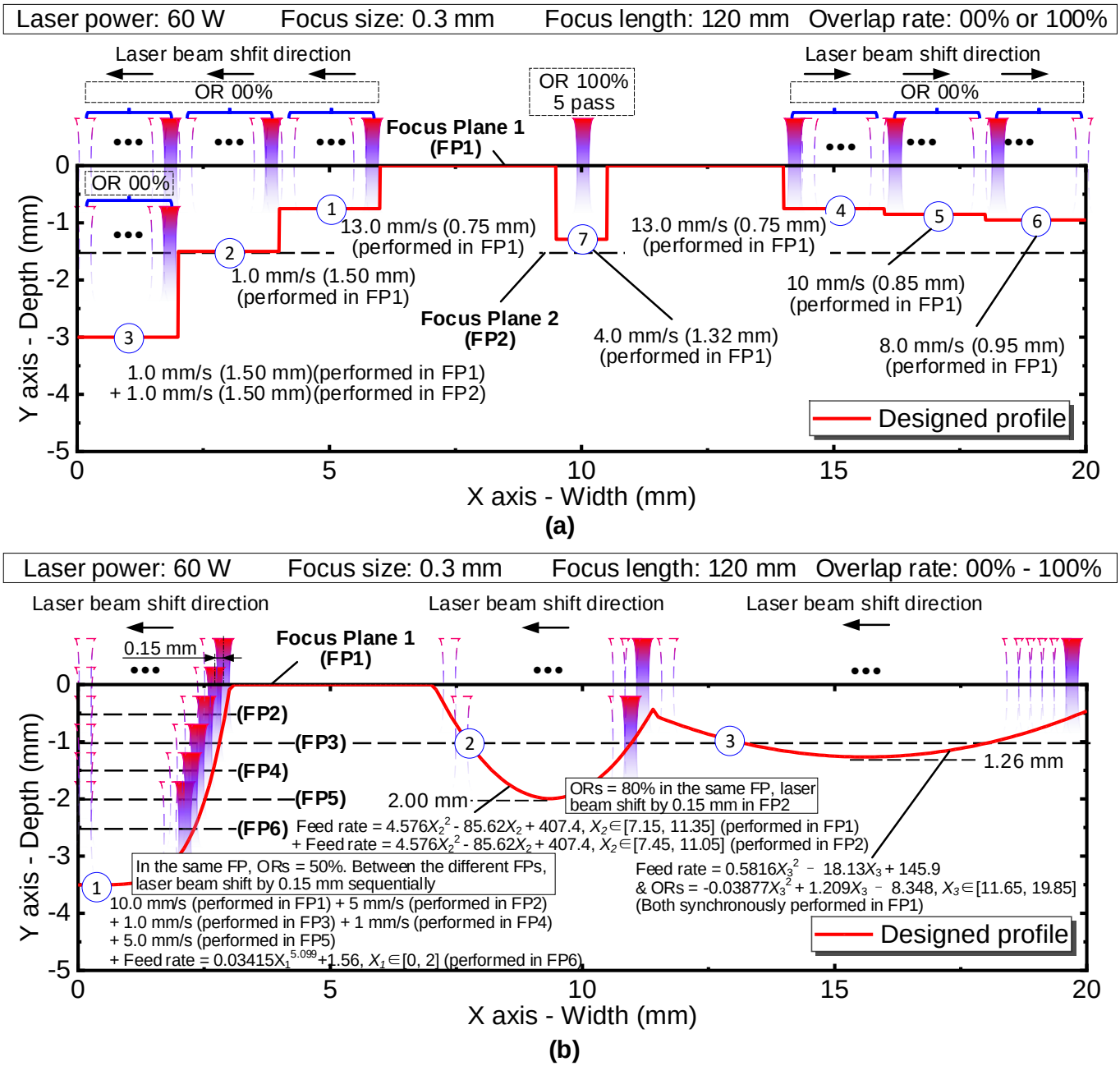

Fig. 13 Planned ablation strategies for designed non-flat grinding wheels. (a) strategies on multi-steps wheel featured with large-span macro-steps (steps tagged with No. 1, 2 and 3), deep-narrow slot (slot tagged with No. 7) and high-resolution micro-steps (steps tagged with No. 4, 5 and 6); (b) curved-surfaces wheel featured with exponential (surfaces tagged with No. 1), parabolic (surfaces tagged with No. 2) and arcuate (surfaces tagged with No. 3) generatrix.

To be specific, **Fig. 13** (a) shows the details of strategies on a multi-step wheel, which featured large-span macro-steps (steps tagged with No. 1, 2 and 3), deep-narrow slot (slot tagged with No. 7) and high-resolution micro-steps (steps tagged with No. 4, 5 and 6). Wherein, steps tagged with No. 1 to No. 6 are carried out under overlap rate 00% while step tagged with No. 7 is carried out under overlap rate 100% for 5 repeated passes. Meanwhile, except step tagged with No. 3 is ablated in two different focal planes (the ablated surface in focal plane 1 is carefully cleaned before the ablation process in focal plane 2), all the other steps are ablated in focal plane 1. **Fig. 13** (b) reveals the strategies on a curved-surfaces wheel featured with exponential (surface tagged with No. 1), parabolic (surface tagged with No. 2) and arcuate (surface tagged with No. 3)

generatrix. Wherein, exponential generatrix (surface tagged with No. 1) is generated with 6 times FP change. In the first 5 FPs, an overlap rate of 50% (the adjacent two passes will not cause the ablation depth to dramatically increase) is employed in the same FP and the laser beam shift by 0.15 mm (the radius of the focus spot) sequentially between the FPs to adjust the positions and focal planes. Additionally, several fixed scanning speed is assigned to the laser beam in different focal planes (10.0 mm/s, 5.0 mm/s, 1.0 mm/s, 1.0 mm/s, 5.0 mm/s and a function controlled speed which is formulated according to the errors between the current and the target ablation depth, respectively). The parabolic generatrix (surface tagged with No. 2) is generated with 2 times FP change and both the two FPs (FP1 and FP3) use the same ORs of 80% (the ablated profile achieved in this OR is similar to the target profile) and the same functional feed rate designed according to the target profile. Differently, the arcuate (surface tagged with No. 3) generatrix is generated in the same FP, while the feed rate and ORs are synchronously changed along the target profile to get the final ablation result (the maximum depth of this profile is capable enough for one-time ablation forming). It is worth mentioning that the ablated surfaces are carefully cleaned with a hairbrush to minimize the effect of attachments when multiple FPs is employed. A 0.15 mm length is reserved for both the ends in each focal plane as the HAZ will remove the unwanted materials.

After the whole ablation process, the achieved grinding wheel is carefully cleaned with a hairbrush and ultrasonic distilled water bath for an hour, and a sample is taken from the wheel and polished. Then the cross-section profile of the grinding wheel sample is photographed by optical microscopy and measured by a laser distance measurement sensor, and the comparisons between the measured and designed target profiles are presented in **Fig. 14**.

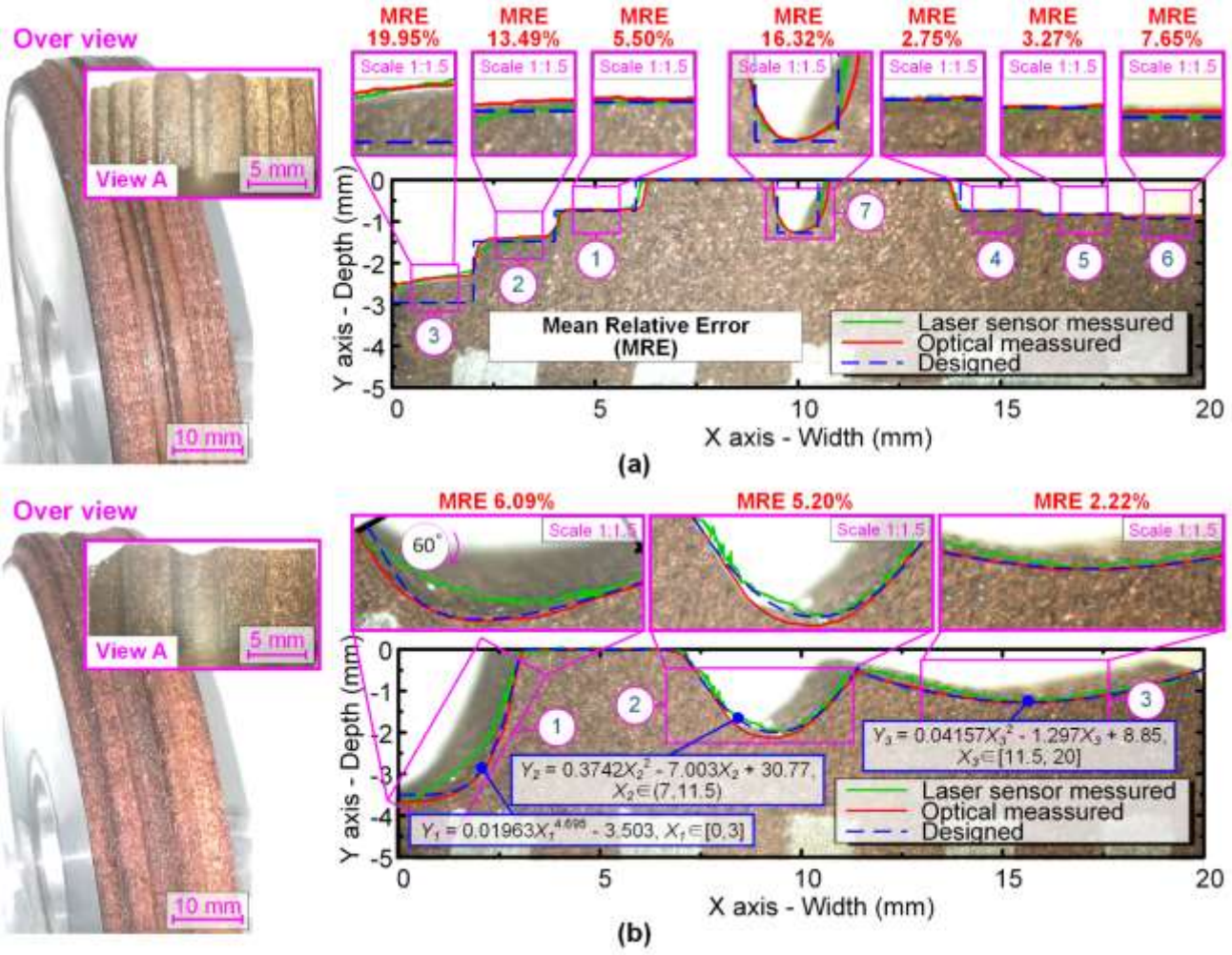

Fig. 14 Ablation results using proposed strategies. (a) multi-steps profile wheel featured with large-span macro-steps (steps tagged with No. 1, 2 and 3), deep-narrow slot (slot tagged with No. 7) and high-resolution micro-steps (steps tagged with No. 4, 5 and 6); (b) curved-surfaces profile wheel featured with exponential (surfaces tagged with No. 1), parabolic (surfaces tagged with No. 2) and arcuate (surfaces tagged with No. 3) generatrix.

Fig. 14 (a) shows the Mean Relative Error (MRE) for the comparison of the optical measurement and designed results of the multi-step profile wheel. It shows the errors increased with steps aimed at deeper ablation depth, like step tagged with No. 3 aimed -3.00 mm has the error of 19.95% (the maximum error), step tagged with No. 2 aimed -1.5 mm has the error of 13.49%, while steps tagged with No. 1 and No. 4 both aimed -0.75 mm achieved the errors of 3.06% and 2.75% respectively. For these steps achieved in the same focal plane tagged with No. 1, No. 2, No. 4, No. 5 and No. 6, the errors are likely to stem from the off-focus effect of the laser beam causing the imperfect of the prediction model. Meanwhile, the step tagged with No. 7 is also suffered from the nature of the laser beam energy distribution as described in **Fig. 1** (c). For step tagged with No. 3 achieved with the adjustment of the focal plane may be suffered from both the off-focus effect and the potential graphitisation effect due to the heat effect from the previous pass that makes the target materials hard to remove.

As inspired by the ablation results from **Fig. 14** (a) that the errors can be restrained when the ablation depth is shallow. Therefore, **Fig. 14** (b) shows the results after an adjustment for the ablation strategies that performed the ablation process by using multiple focal planes to control

the ablation depth for each ablation step. Amazingly, the overall error for the results of the curved surfaces is dramatically decreased, where the biggest error is 7.03% for the curved surface tagged with No. 1 and followed by 6.83% for the surface tagged with No. 2. As a contrast, the most pleasant results would be the surface tagged with No. 3 that only a 2.22% error is found. The errors from surfaces tagged with No.1 and No. 2 that are likely due to the adjustment of the focal plane make the laser energy easily arrive at the target materials, which causes some of the materials over removed with the laser beam multiple passes on the ablated surfaces. The pleasant result from the surface tagged with No. 3 could attribute to (i) the relatively small ablation depth makes it no necessity to change the focal plane, (ii) the synchronously change of both the feed rate and ORs that makes it capable to cover all the designed key points, and (iii) the relatively smooth profile makes the platform possible to response all the set processing parameters.

Overall, the measured results by both the optical microscopy and the laser distance measurement sensor showed great consistency with the proposed model (as shown in **Fig. 14**). However, some discrepancies were found between the two different measurement methodologies, especially in the measured results for surface tagged with No. 1 in **Fig. 14** (b) - the maximum discrepancy exceeds 28%. Two reasons may account for the discrepancies: (i) the profile boundaries can be easily recognised by optical method, but as some deteriorated material is still attached to the matrix, they cannot be distinguished by the laser measurement sensor. Therefore, the measurement accuracy for the laser distance measurement sensor is closely related to the quality of cleaning applied to the HAZ; (ii) the surface tagged with No. 1 in **Fig. 14** (b) featured the largest ablation depth and curved surface, and is manufactured with multiple focal plane changes and feed rate parameter adjustments, leading to a larger and less predictable HAZ.

5 Conclusions

In this study, both theoretical and experimental work is carried out to investigate the possibilities of manufacturing the high-resolution profiled grinding wheel by controlling the focal plane, ORs and feed rate change. Generally, the key conclusions drawn from the paper can be summarized as below:

1) The natures and the characters of the laser beam ablation are analysed, based on the analysis, the possibilities of manufacturing the profiled grinding wheel by controlling the ORs are theoretically analysed and experimentally proved. It revealed that for the given laser conditions, the ablation depth will not be obviously increased when the overlap rate is below 50% for the nature of laser beam energy super-Gauss distribution, and even if the overlap rate is 100%, the ablation depth will also not be continuously increased for the off-focus effect.

2) The ablation law regarding ablated depth, width, and topography changes with overlap rate and feed rate is studied, and the corresponding empirical prediction models are established. Meanwhile, the errors for the prediction models are also analysed. It shows the ablation depth is kept almost unchanged when the overlap rate is lower than 50% and the ablation depth begins to grow obviously when the overlap rate is over 50%. The average drop for all feed rates is 0.24 mm with a maximum variation of 0.06 mm under the trailed ORs that indicate the feed rates affect almost equally the ablation depth. In the worst situation, the established prediction model still has the R-square result of 89%, which indicated the effectiveness of the model.

3) An application attempt to generate precise non-flat surfaces like stepped surfaces and curved surfaces by using the CO2 laser generator has been demonstrated, which showed the pleasant result can be achieved by the developed strategies in this study. It shows with the synchronous change of both the feed rate and ORs, a relatively smooth profile with a relative error of 2.22% can be achieved without extra focus plane changes (an effective way to avoid unexpected errors resulting from the off-focus effect when deeper ablation depth is required).

Acknowledgements

The authors acknowledge the support of the University of Nottingham, Ningbo, China (I02201000002, I01201200027).

References

[1] Miao Q, Ding WF, Kuang WJ, Xu JH. Tool wear behavior of vitrified microcrystalline alumina wheels in creep feed profile grinding of turbine blade root of single crystal nickel-based superalloy. Tribol Int 2020;145:1-10. https://doi.org/10.1016/j.triboint.2019.106144.
[2] Li X, Qin B, Wang ZM, Zhang Y, Yu JH. Grinding of fir tree slots of powder metallurgy superalloy FGH96 using profiled electroplated CBN wheel. Int J Adv Manuf Tech 2021;115:311–317. https://doi.org/10.1007/s00170-021-07179-z.
[3] Christian Waltera, Tim Komischkea, Eduardo Weingärtnerb, Wegenera K. Structuring of CBN grinding tools by ultrashort pulse laser ablation. CIRP 2014;2014:31-36. https://doi.org/10.1016/j.procir.2014.03.093.
[4] Hsue AWJ, Chang YF. Toward synchronous hybrid micro-EDM grinding of micro-holes using helical taper tools formed by Ni-Co/diamond Co-deposition. Journal of Materials Processing Technology 2016;234:368-382. http://dx.doi.org/10.1016/j.jmatprotec.2016.04.009.
[5] Thang VT, Tuan NA, Tiep NV. Evaluation of grinding wheel wear in wet profile grinding for the groove of the ball bearing's inner ring by pneumatic probes. J Mech Sci Technol 2018;32:1297-1305. https://doi.org/10.1007/s12206-018-0234-5.
[6] Fang CG, Gong JM, Guo EK, Zhang H, Huang XD. Analysis and Compensation for Gear Accuracy with Setting Error in Form Grinding. Adv Mech Eng 2015;21:716-723. https://doi.org/10.1155/2014/309148.
[7] Liu XR, Wang ZH. Research on High-Precision Form Grinding Technology of Gear Based on Ambient Temperature Adaptability. Math Probl Eng 2018;2018:1-13. https://doi.org/10.1155/2018/4619624.
[8] Miao Q, Ding WF, Kuang WJ, Yang CY. Grinding force and surface quality in creep feed profile grinding of turbine blade root of nickel-based superalloy with microcrystalline alumina abrasive wheels. Chinese Journal of Aeronautics 2021;34:576-585. https://doi.org/10.1016/j.cja.2019.11.006.
[9] Nguyen DT, Nguyen HA, Lee AC. Design of grinding wheel profile for new micro drill flute. T Can Soc Mech Eng 2018;42:116-124. https://doi.org/10.1139/tcsme-2017-0048.
[10] Tao LJ, Xing Y, Yuan MX, Chen SJ. A correction method of screw rotor profile error based on parameter adjustment for grinding wheel dresser. Adv Mech Eng 2018;10:1-7. https://doi.org/10.1177/1687814018798977.
[11] Chen SS, Yang SM, Liao ZR, Cheung CF, Jiang ZD, Zhang FH. Curvature effect on surface topography and uniform scallop height control in normal grinding of optical curved surface considering wheel vibration. Opt Express 2021;29:8041-8063. https://doi.org/10.1364/Oe.418599.
[12] Wang S, Zhao Q, Guo B, Pan Y. Ultra-precision raster grinding of monocrystalline silicon biconical free-form optics using arc-shaped diamond grinding wheels. J Manuf Process 2020;58:1064-1074. https://doi.org/10.1016/j.jmapro.2020.09.020.
[13] Wang W, Zhang Z, Yao P, Wang XY, Zhang ZB, Liu YH. Envelope grinding of micro-cylinder

array lenses using a near arc-profile wheel without on-machine precision truing. Journal of Materials Processing Technology 2021;289. https://doi.org/10.1016/j.jmatprotec.2020.116927.
[14] Chen SY, Wu CC, Xue S, Li ZJ. Fast registration of 3D point clouds with offset surfaces in precision grinding of free-form surfaces. Int J Adv Manuf Tech 2018;97:3595-3606. https://doi.org/10.1007/s00170-018-2203-7.
[15] Zhang ZX, Fong ZH. A novel tilt form grinding method for the rotor of dry vacuum pump. Mech Mach Theory 2015;90:47-58. https://doi.org/10.1016/j.mechmachtheory.2015.02.005.
[16] Li G, Wang ZH, Zhu WD, Kubo A. A function-oriented active form-grinding method for cylindrical gears based on error sensitivity. Int J Adv Manuf Tech 2017;92:3019-3031. https://doi.org/10.1007/s00170-017-0363-5.
[17] Su JX, Ke QX, Deng XZ, Ren XZ. Numerical simulation and experimental analysis of temperature field of gear form grinding. Int J Adv Manuf Tech 2018;97:2351-2367. https://doi.org/10.1007/s00170-018-2079-6.
[18] Wang L, Tian XL, Liu Q, Li YD, Tang XJ, Yang LJ. Experimental study and theoretical analysis of the form grinding of gears using new type micro-crystal corundum grinding wheels. Int J Adv Manuf Tech 2017;92:1659-1669. https://doi.org/10.1007/s00170-017-0246-9.
[19] Jin T, Yi J, Li P. Temperature distributions in form grinding of involute gears. Int J Adv Manuf Tech 2017;88:2609-2620. https://doi.org/10.1007/s00170-016-8971-z.
[20] Yi J, Jin T, Deng ZH. The temperature field study on the three-dimensional surface moving heat source model in involute gear form grinding. Int J Adv Manuf Tech 2019;103:3097-3108. https://doi.org/10.1007/s00170-019-03752-9.
[21] Yi J, Jin T, Zhou W, Deng ZH. Theoretical and experimental analysis of temperature distribution during full tooth groove form grinding. J Manuf Process 2020;58:101-115. https://doi.org/10.1016/j.jmapro.2020.08.011.
[22] Yi J, Jin T, Deng ZH, Zhou W. Estimation of residual stresses in gear form grinding using finite element analysis and experimental study based on grinding force and heat flux distribution models. Int J Adv Manuf Tech 2019;104:849-866. https://doi.org/10.1007/s00170-019-03825-9.
[23] Zhao ZC, Fu YC, Xu JH, Zhang ZW, Liu ZW, He J. An investigation on high-efficiency profile grinding of directional solidified nickel-based superalloys DZ125 with electroplated CBN wheel. Int J Adv Manuf Tech 2016;83:1-11. https://doi.org/10.1007/s00170-015-7550-z.
[24] Zhang YH, Wu Q, Hu DJ. Research on wear detection of wheel in precision NC curve point grinding. Int J Adv Manuf Tech 2008;35:994-999. https://doi.org/10.1007/s00170-006-0783-0.
[25] Liao JY, Xie J, Yang H, Sun JX. Modeling of curved diamond wheel errors for improvement of freeform grinding accuracy. Int J Adv Manuf Tech 2019;103:1879-1892. https://doi.org/10.1007/s00170-019-03679-1.
[26] Starkov VK, Ryabtsev SA, Polkanov EG, Kiskin OS. Comparative analysis of performance of cubic boron nitride and microcrystalline alumina tools in profile grinding of form cutters. J Superhard Mater+ 2014;36:43-48. https://doi.org/10.3103/S1063457614010079.
[27] Xie J, Zhou RM, Xu J, Zhong YG. Form-truing error compensation of diamond grinding wheel in CNC envelope grinding of free-form surface. Int J Adv Manuf Tech 2010;48:905-912. https://doi.org/10.1007/s00170-009-2338-7.
[28] Xie J, Zheng JH, Zhou RM, Lin B. Dispersed grinding wheel profiles for accurate freeform surfaces. Int J Mach Tool Manu 2011;51:536-542. https://doi.org/10.1016/j.ijmachtools.2011.03.002.
[29] Xie J, Deng ZJ, Liao JY, Li N, Zhou H, Ban WX. Study on a 5-axis precision and mirror grinding of glass freeform surface without on-machine wheel-profile truing. Int J Mach Tool Manu 2016;109:65-73. https://doi.org/10.1016/j.ijmachtools.2016.07.011.
[30] Yang JH, Zhang DH, Wu BH, Zhang Y, Luo M. A path planning method for error region grinding of aero-engine blades with free-form surface. Int J Adv Manuf Tech 2015;81:717-728. https://doi.org/10.1007/s00170-015-7186-z.
[31] Qi JD, Chen B. Elastic-contact-based tool-path planning for free-form surface in belt grinding. Adv Mech Eng 2019;11. https://doi.org/10.1177/1687814018819921.

[32] Bogutsky V, Novoselov Y, Shron L. Calculating the profile of intermittent grinding wheel for the sharpening teeth of the broach. Matec Web Conf 2018;224. https://doi.org/10.1051/matecconf/201822401003.
[33] Ichida Y. Profile Grinding of High-Speed Steel using Ultrafine-Crystalline cBN Wheels. J Adv Mech Des Syst 2008;2:385-395. https://doi.org/10.1299/jamdsm.2.385.
[34] Liu ZM, Tang Q, Liu N, Liang PH, Liu W. A Novel Optimization Design Method of Form Grinding Wheel for Screw Rotor. Appl Sci 2019;9. https://doi.org/10.3390/app9235079.
[35] Deng H, Xu Z. Dressing methods of superabrasive grinding wheels: A review. J Manuf Process 2019;45:46-69. https://doi.org/10.1016/j.jmapro.2019.06.020.
[36] Denkena B, Krodel A, Gartzke T. Process design of the patterning process of profile grinding wheels. Proc Cirp 2019;86:126-132. https://doi.org/10.1016/j.procir.2020.01.011.
[37] Axinte DA, Stepanian JP, Kong MC, McGourlay J. Abrasive waterjet turning-An efficient method to profile and dress grinding wheels. Int J Mach Tool Manu 2009;49:351-356. https://doi.org/10.1016/j.ijmachtools.2008.11.006.
[38] Deng H, Chen GY, He J, Zhou C, Du H, Wang YY. Online, efficient and precision laser profiling of bronze-bonded diamond grinding wheels based on a single-layer deep-cutting intermittent feeding method. Opt Laser Technol 2016;80:41-50. https://doi.org/10.1016/j.optlastec.2015.12.021.
[39] Guo B, Meng Q, Li S, Wu G, Xiang Y, Zhao Q. Pulse laser precision truing of the V-shaped coarse-grained electroplating CBN grinding wheel. Mater Design 2022;217:110650. https://doi.org/10.1016/j.matdes.2022.110650.
[40] Rushworth AGA, Xie KG, Fang BL, Shen YX, Huang ZP, Zhang XY. Generating Profiled Diamond Grinding Wheels by 2000 W Fiber Laser: On The Understanding of Laser Ablation Law with High Power and Establishment of a Predictive Model. The International Journal of Advanced Manufacturing Technology 2022;120:3045-3063. https://10.1007/s00170-022-08934-6.
[41] Aurich JC, Herzenstiel P, Sudermann H, Magg T. High-performance dry grinding using a grinding wheel with a defined grain pattern. CIRP Annals 2008;57:357-362. https://doi.org/10.1016/j.cirp.2008.03.093.
[42] Ding WF, Xu JH, Chen ZZ, Miao Q, Yang CY. Interface characteristics and fracture behavior of brazed polycrystalline CBN grains using Cu–Sn–Ti alloy. Mater. Sci. & Eng.: A 2013;559:629-634. https://doi.org/10.1016/j.msea.2012.09.002.
[43] Chen J, Fu Y, Li Q, Gao J, He Q. Investigation on induction brazing of revolving heat pipe grinding wheel. Mater. Design 2017;116:21-30. https://doi.org/10.1016/j.matdes.2016.11.057.
[44] Huang G, Huang J, Zhang M, Mu D, Zhou G, Xu X. Fundamental aspects of ultrasonic assisted induction brazing of diamond onto 1045 steel. J. Mater. Process Tech. 2018;260:123-136. https://doi.org/10.1016/j.jmatprotec.2018.05.021.
[45] Li QL, Ding K, Lei WN, Chen JJ, He QS, Chen ZZ. Investigation on induction brazing of profiled cBN wheel for grinding of Ti-6Al-4V. Chinese Journal of Aeronautics 2021;34:132-139. https://doi.org/10.1016/j.cja.2020.07.0401000-9361.
[46] Yu H, Lyu Y, Wang J, Wang X. A biomimetic engineered grinding wheel inspired by phyllotaxis theory. Journal of Materials Processing Technology 2018;251:267-281. https://doi.org/10.1016/j.jmatprotec.2017.08.041.
[47] Zhao B, Guo X, Bie W, Chang B, Zhao C. Thermo-mechanical coupling effect on surface residual stress during ultrasonic vibration-assisted forming grinding gear. J Manuf Process 2020;59:19-32. https://doi.org/10.1016/j.jmapro.2020.09.041.
[48] Guo B, Zhang J, Wu M, Zhao Q, Liu H, Monier A, Wang J. Water assisted pulsed laser machining of micro-structured surface on CVD diamond coating tools. J Manuf Process 2020;56:591-601. https://doi.org/10.1016/j.jmapro.2020.04.066.
[49] Guo Z, Guo B, Zhao Q, Liu W, Zheng Q. Optimisation of spray-mist-assisted laser machining of micro-structures on CVD diamond coating surfaces. Ceramics International 2021;47:22108-22120. https://doi.org/10.1016/j.ceramint.2021.04.232.
[50] Xu LM, Fan F, Zhang Z, Chao XJ, Niu M. Fast on-machine profile characterization for grinding

wheels and error compensation of wheel dressing. Precis Eng 2019;55:417-425. https://doi.org/10.1016/j.precisioneng.2018.10.010.
[51] Shealy DL, Hoffnagle JA. Laser beam shaping profiles and propagation. Applied Optics 2006;45:272944773. https://doi.org/10.1364/ao.45.005118.
[52] Wu J, Wei H, Yuan F, Zhao P, Zhang Y. Effect of beam profile on heat and mass transfer in filler powder laser welding. Journal of Materials Processing Technology 2018;258:47-57. https://10.1016/j.jmatprotec.2018.03.011.
[53] Bellini N, Geremia R, Karnakis D. Increasing laser pulse overlap restricts picosecond laser ablation of thin metal films near ablation threshold. Appl Phys a-Mater 2017;123. https://doi.org/10.1007/s00339-017-0971-9.
[54] Wang FB, Liu MZ, Tu P. Analysis of overlapping rate of spot derived from ablated monocrystalline silicon by femtosecond laser. J Laser Appl 2020;32. https://doi.org/10.2351/7.0000183.
[55] Beausoleil C, Sarvestani HY, Katz Z, Gholipour J, Ashrafi B. Deep and high precision cutting of alumina ceramics by picosecond laser. Ceramics International 2020;46:15285-15296. https://doi.org/10.1016/j.ceramint.2020.03.069.
[56] Schnell G, Duenow U, Seitz H. Effect of Laser Pulse Overlap and Scanning Line Overlap on Femtosecond Laser-Structured Ti6Al4V Surfaces. Materials 2020;13. https://doi.org/10.3390/ma13040969.
[57] Zimmer K, Ehrhardt M, Lorenz P, Wang X, Vass C, Csizmadia T, Hopp B. Reducing the incubation effects for rear side laser etching of fused silica. Appl Surf Sci 2014;302:42-45. https://doi.org/10.1016/j.apsusc.2014.01.115.
[58] Li HN, Xie KG, Wu B, Zhu WQ. Generation of textured diamond abrasive tools by continuous-wave CO2 laser: Laser parameter effects and optimisation. Journal of Materials Processing Technology 2020;275:116279. https://10.1016/j.jmatprotec.2019.116279.
[59] Ding ZH, Cui FK, Liu YB, Li Y, Xie KG. A Model of Surface Residual Stress Distribution of Cold Rolling Spline. Math Probl Eng 2017;2017:1-21. https://doi.org/10.1155/2017/2425645.